Coupling 2D atomistic information to 3D kink-pair enthalpy models of screw dislocations in bcc metals

Sicong He,[1] Emma Overly,[1] Vasily Bulatov,[2] Jaime Marian,[1,3,*] and David Cereceda[4]

[1]*Department of Materials Science and Engineering, University of California Los Angeles, Los Angeles, California 90095, USA*
[2]*Physical and Life Sciences Directorate, Lawrence Livermore National Laboratory, Livermore, California 94550, USA*
[3]*Department of Mechanical and Aerospace Engineering, University of California Los Angeles, Los Angeles, California 90095, USA*
[4]*Department of Mechanical Engineering, Villanova University, Villanova, Pennsylvania 19085, USA*

(Received 14 April 2019; published 15 October 2019)

The kink-pair activation enthalpy is a fundamental parameter in the theory of plasticity of body-centered cubic (bcc) metals. It controls the thermally activated motion of screw dislocation at low and intermediate temperatures. While direct atomistic calculations of kink pairs on screw dislocations have reached a high degree of accuracy, they can only be practically performed using semiempirical interatomic force fields, as electronic structure methods have not yet reached the level of efficiency needed to capture the system sizes required to model kink-pair structures. In this context, an alternative approach based on standard three-dimensional elastic models, which are efficient but lack atomic-level information, coupled to a substrate potential that represents the underlying lattice, has been widely applied over the past few years. This class of methods, known as 'line-on-substrate' (LOS) models, uses the substrate potential to calculate the lattice contribution to the kink-pair energies. In this work, we introduce the stress dependence of the substrate potential into LOS models to evaluate its impact on kink-pair energies. In addition, we include asymmetric dislocation core energies as an extra descriptor of the dislocation character. This asymmetry is also elevated to the continuum level by adding core energies to the general LOS formulation and used to explain potential energy differences known to exist between left and right kinks in bcc metals. More importantly, by matching the total LOS energies to previously calculated atomistic energies of kink-pair configurations, we issue a rule to establish the value of the so-called *core width* in nonsingular elasticity theories and reduce its arbitrariness as a mathematical construct.

DOI: 10.1103/PhysRevMaterials.3.103603

I. INTRODUCTION

In the field of dislocation physics, body-centered cubic (bcc) metals are peculiar due to the existence of nonplanar dislocations with screw character and thermally-activated mobility that control plastic flow at low-to-intermediate temperatures. These dislocations have a Burgers vector $\boldsymbol{b}$ equal to $\frac{1}{2}\langle 111\rangle$ and move on close-packed planes (primarily {110} and {112}) [1–5]. Generally, this motion is understood to occur over a periodic energy landscape known as the *Peierls* potential via the thermally activated nucleation of steps on the dislocation line, known as *kink pairs*, and their subsequent sideward relaxation [6–12]. Screw dislocations in bcc materials often behave in noncrystallographic ways, giving rise to phenomena such as pencil glide, asymmetry of the critical stress in the twinning and antitwinning glide directions, asymmetry of the critical stress under tension/compression loading, or anomalous slip [13–23]. Most of these peculiarities are typically attributed to the highly compact (nonplanar) structure of the $\frac{1}{2}\langle 111\rangle$ screw dislocation core, which has naturally attracted much attention over the last several decades mostly in the form of atomistic models [24–26]. Based on recent work using electronic structure calculations, a picture has emerged whereby the preferred dislocation core structure in bcc crystals has been established to be a compact, nondissociated core resting on an underlying sinusoidal Peierls potential, U_{P} [27–31].

The strong temperature dependence of the yield and flow stresses displayed by most bcc metals is generally rationalized in terms of the thermally-activated nature of kink-pair nucleation. As such, a principal objective of the materials community in bcc alloys has been to develop models to characterize the activation energy of kink pairs. These are typically based on energy minimization of curved string configurations lying on a static energy substrate in either one [32,33] or two dimensions [34]. The energy of the string is obtained by solving an integrodifferential equation in a two-dimensional space defined by the glide x and screw z directions that accounts for the elastic energy of the line, its position on the substrate potential, and the mechanical work done by the stress τ [35,36]. These so-called *line-on-substrate* (LOS) approaches have been traditionally approximated by models that reduce the double line integral (along x and z) to discrete sums along one or both integration dimensions. In the so-called line-tension (LT) model the integral along the screw direction is replaced by a dislocation self-energy which depends on the curvature of the line. The other integral is solved along the glide coordinate, yielding the equilibrium shape of the kink-pair configuration on the substrate potential.

*jmarian@ucla.edu

These activated configurations are usually referred to as 'bulge' structures as they resemble a protuberance on the dislocation line projected along the glide direction. The LT approach works well when this protuberance is small, i.e., at high and intermediate stresses,[1] but not at low stresses when the equilibrium position of the line is near the minimum of potential energy U_P [32,33]. For low values of τ, the elastic interaction (EI) between kinks governs the line energy, in which case one can approximate the bulge configuration by a polygon (typically a trapezoid) with mutually-interacting elastic segments, reducing the double integral to a set of discrete convergent sums [37,38]. While this is a general consideration, irrespective of the material and the dislocation type, the case of screw dislocations in tungsten does not really follow this idea. This is because nonscrew segments of the trapezoid are highly tilted towards the screw character (which is a consequence of the core energy values and not uncommon in bcc metals).

While insights gained from these models have improved our understanding of the activated states of kink-pair configurations, knowledge obtained from a decade or so of atomistic calculations supports the need to augment LOS models with inelastic contributions brought about by nonlinear effects of atomistic nature. The most important of these are (i) the alteration of the Peierls potential energy function in the presence of resolved shear stress and (ii) the consideration of core energies into the energy description of kink-pair configurations. At low stresses, one can safely assume that U_P remains unchanged and the effect of stress on the dislocation can be linearly decoupled from the underlying substrate in the form of a mechanical work. However, at stresses approaching the critical stress, referred to as the *Peierls* stress τ_P at 0 K, it is insufficient to consider only the zero stress internal energy to represent the Peierls trajectory. This trajectory is defined as the rectilinear path, denoted by the reaction coordinate x, between two equivalent equilibrium states (known as 'easy core') on the Peierls potential, which has periodicity $h_0 = a_0\frac{\sqrt{6}}{3}$, where a_0 is the lattice constant. As recent calculations have shown, U_P can couple to the applied stress in non-negligible ways [39]. For its part, the inelastic contribution to the total dislocation energy, referred to as the *core* energy, is known to be potentially an important driving force in the minimization of dislocation line configurations (e.g., the so-called *self-force* in dislocation dynamics models). In particular, as will be shown below, in bcc metals the dependence of the core energy with dislocation character is periodic in the entire $[-\frac{\pi}{2}, \frac{\pi}{2}]$ angular range of θ (taken to be equal to zero for the screw orientation), contrary to other crystal structures, which display a $[0, \frac{\pi}{2}]$ periodicity. While this is a consequence of a well-known asymmetry of the bcc crystal lattice [4,15,16], it has not been included into continuum models of kink-pair configurations to date.

In this work, we explore the effect of these features on numerical LT and EI models of kink-pair configurations modified to account for variations in $U_P(x)$ brought about by the applied stress and character-dependent dislocation core energies. Ultimately, we are testing the notion of whether atomistic information based on (quasi-)2D simulations can be effectively integrated into dislocation energy models of 3D line configurations is correct to interpret bcc plastic behavior. As well, we check whether fine details obtained in atomistic models, such as, e.g., the energy asymmetry between left and right-handed kinks that has been observed in several bcc metals [40–42], can be accurately captured by this coupled approach. Our paper is organized as follows. First we introduce the unprocessed physical inputs as obtained from atomistic simulations. Next, we review the theoretical formulation of the EI and LT models employed here. This is followed by details about the coupling between atomistic information and the discretized continuum models. We then show results for two different atomistic force fields for tungsten. We conclude the paper with a discussion of the results and some general conclusions.

II. RAW ATOMISTIC INPUTS

Based on a prior analysis of several W interatomic potentials for screw dislocation property calculations [43], we have selected an embedded-atom method (EAM) [44] and a *modified*-EAM (MEAM) potential [45] as the most suitable in terms of physical accuracy and computational efficiency. Using these two potentials, we have studied the dependence of $U_P(x)$ on the resolved shear stress and of the dislocation core energies on dislocation character. This furnishes what we refer to as 'raw' atomistic inputs, i.e., before they are processed to be in usable form for the LOS models.

A. Peierls potential

The Peierls potential $U_P(x)$ is obtained as the minimum energy path along the reaction coordinate x joining two adjacent equilibrium dislocation core configurations (known as *easy* core configurations). This is done using the *nudged elastic band* (NEB) method [46] in small atomistic supercells reflecting the structure of balanced dipole configurations oriented along the [111], $[\bar{1}2\bar{1}]$, and $[\bar{1}01]$ directions, corresponding, respectively, to the x, y and z directions. These configurations permit the use of periodic boundary conditions along all three supercell directions. The dimensions of the simulation cell along the three coordinate axes were $L_x = 13.6$ Å $(5b)$, $L_y = 108$ Å, and $L_z = 107$ Å, containing a total of $N = 10\,000$ atoms. The NEB trajectory is partitioned into 30 images constrained to relax in configurational hyperplanes defined by the normal axis along x $(3N - 1$ degrees of freedom).

Prior to the NEB calculations, unconstrained energy minimizations using LAMMPS [47] were carried out for the initial and final configurations. NEB trajectories are generated as a function of stress τ (resolved shear stress on the glide plane) and the results are shown in Fig. 1. The paths shown in the figure are generated by subtracting from the resulting NEB trajectory the mechanical work, $-\tau bx$, for each image and matching the equilibrium position, $x_0(\tau)$, and the associated energy in each case to the origin of each curve.

[1]While the terms 'low' and 'high' stress used throughout this paper are somewhat arbitrary, here, for reference, we have decided to assign a value of $0.25\sigma_P$ as the high limit of the low stress region and $0.75\sigma_P$ as the low limit of the high stress region.

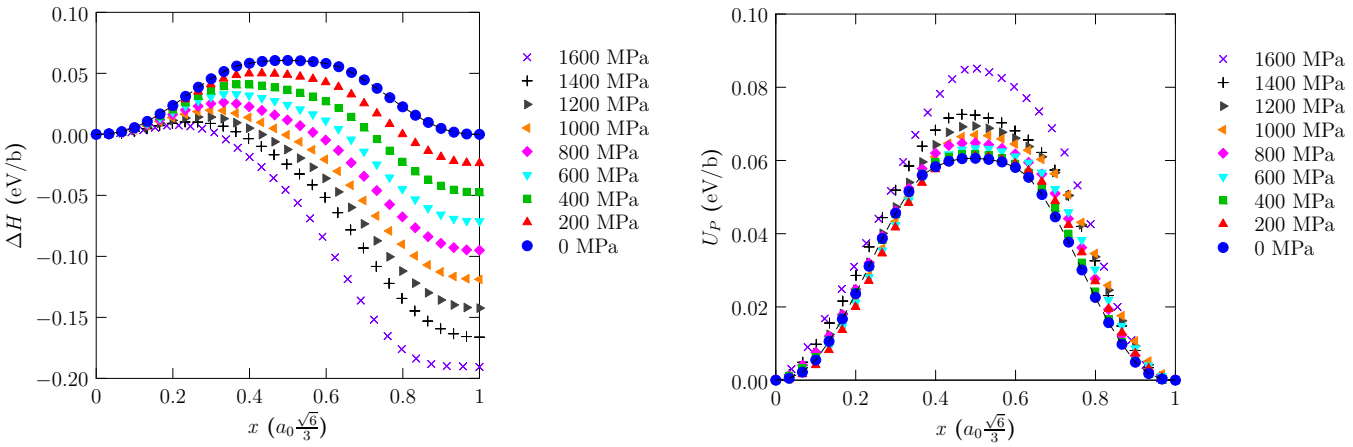

FIG. 1. Variation of (a) the enthalpy and (b) the Peierls potential with stress for the EAM potential. Graphs (a) and (b) are connected by the term $-\tau b$, which is subtracted to the enthalpy to obtain U_{P}.

B. Dislocation core energies

The dislocation core energy is a mathematical construct designed to remove the singularity in the stress and strain fields of elasticity theory. As such, the core region is eminently *inelastic* in nature and can arbitrarily be defined by a parameter a referred to as the *core width*. This effectively partitions the total energy of a dislocation dipole into elastic and inelastic parts, with the latter confined to the core region within a [48–50] (cf. Sec. III A 2). This partition results in the following definition of the core energy:

$$e_c(\theta, a) = \frac{e_{\mathrm{atm}}(\theta) - e_{\mathrm{el}}(\theta, a)}{2} \tag{1}$$

where the angle $\theta = \cos^{-1}\left(\frac{\boldsymbol{b}\cdot\boldsymbol{t}}{b}\right)$ formed by the Burgers vector $\boldsymbol{b}$ and the line direction $\boldsymbol{t}$ defines the dislocation character, while the $1/2$ factor reflects the existence of a dislocation dipole.

The total energy e_{atm} is obtained from conjugate gradient minimizations of periodic atomistic supercells containing a dislocation dipole much in the manner described in the above section. The only difference resides in the orientation of the supercell, whose axes z, y, and x are now oriented along the $\boldsymbol{n}$, $\boldsymbol{t}$ and $(\boldsymbol{n}\times\boldsymbol{t})$ directions, respectively. For its part, the elastic energy e_{el} is calculated by subtracting the interaction energy due to the periodic dipole network (appearing by virtue of using periodic boundary conditions) from the elastic energy of a dislocation dipole. An example of the partition of energy described by Eq. (1) is shown in Fig. 2. The core energies assuming a value of $a = 2b$ for the EAM and MEAM potentials, as well as for DFT calculations of pure screw (0°) and edge (90°) configurations [51], are also given in Fig. 2. As the graph shows, the angular periodicity of the core energy function is $(0, \pi)$, as there is an asymmetry in the energies about the pure edge orientation. This is not surprising, given the natural crystallographic asymmetry of the bcc lattice, which is most notoriously manifested in the existence of the so-called M111 dislocation orientation [52]. As will be discussed later, this asymmetry in the core energies leads to different energies for 'left' and 'right'-handed kinks, a phenomenon commonly observed in atomistic calculations using a number of interatomic potentials [40–42]. Further details about this geometric particularity are provided in Appendix B.

III. GENERAL THEORY OF THE LINE-ON-SUBSTRATE MODEL

Line-on-substrate model regards the dislocation as a line resting on a periodic energy landscape (substrate) that reflects the coupling between the dislocation line and the crystal lattice. As mentioned in Sec. I, the two most widely used versions of the LOS model are the elastic interaction (EI) model and the line tension (LT) model. Here we provide a description of the theoretical formulations employed here for each of the two cases.

A. Elastic interaction model

In the EI model, a kink pair on a screw dislocation line can be approximated by an open trapezoid connected to two semi-infinite segments in the manner shown in Fig. 3: The segments ***LA*** and ***DR*** are located on the first Peierls valley, the segment ***BC*** is on the second Peierls valley, and ***AB*** and ***CD*** are the kink segments that straddle both minima. w is the width of the trapezoid, which we take to be the distance between kinks, calculated as the distance between the two midpoints of segments ***AB*** and ***CD***. l_1 and l_2 are the widths (along the z direction) of such two segments, calculated as the z distance between the point at $x = 0.05h_0 + x_0$ and that at $x = 0.95h_0 + x_0$. One can use the structure shown in Fig. 3 to obtain stable configurations for the activated state by optimizing the activation enthalpy of the system for a given stress. The activated state can be characterized by the sum of self-energies ΔE_{self} and interaction energies ΔE_{int} for all segments shown in the figure. In addition, the contribution to the energy of the underlying substrate ΔU_{P} must be separately considered for the case of screw dislocations in bcc metals. The enthalpy is then obtained by subtracting the mechanical work W_m performed by the stress τ from the three contributions mentioned above:

$$\Delta H(\{\boldsymbol{r}_i\}, \tau) = \Delta E_{\mathrm{self}}(\{\boldsymbol{r}_i\}, \theta_i) + \Delta E_{\mathrm{int}}(\{\boldsymbol{r}_i\}) + \Delta U_{\mathrm{P}}(\{\boldsymbol{r}_i\}) - W_m(\tau, \{\boldsymbol{r}_i\}). \tag{2}$$

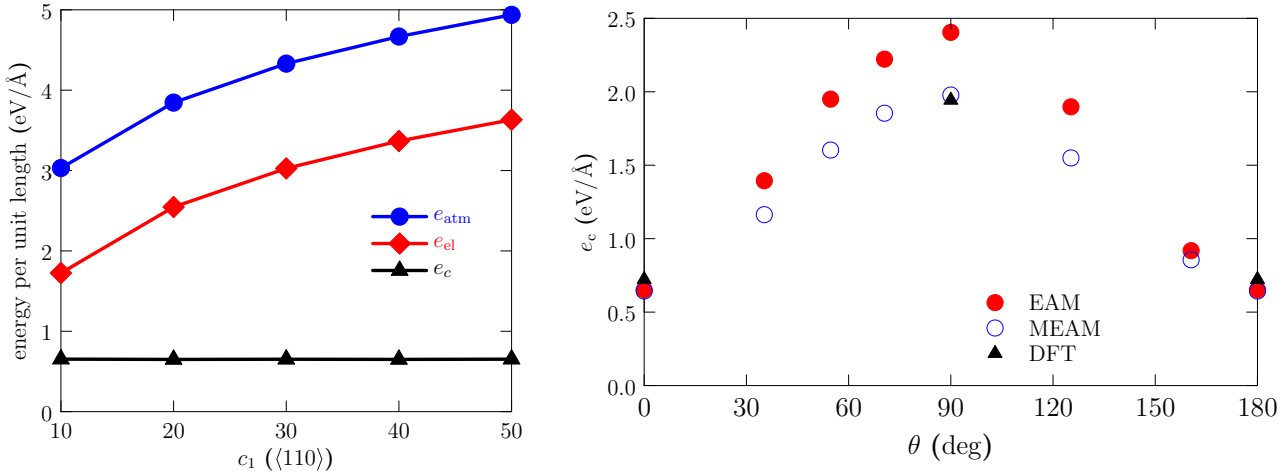

FIG. 2. Core energies obtained from atomistic simulations. (Left) Total atomistic energy (per unit length) for a computational cell containing a screw dislocation segment modeled with the EAM potential. The total energy is partitioned between an elastic energy and a core energy assuming a value of $a = 2b$. c_1 represents the size of the box along a ⟨110⟩ crystallographic direction (separation of the dislocation dipole). (Right) Dislocation core energies as a function of the character angle θ all for $a = 2b$. Results for both interatomic potentials, as well as DFT data, are shown.

The stable configurations for the kink-pair structure shown in the figure are obtained by optimizing the above expression with respect to the coordinates $\boldsymbol{r}_A$, $\boldsymbol{r}_B$, $\boldsymbol{r}_C$, $\boldsymbol{r}_D$. Note that, due to the asymmetry in the e_c function described in the previous section, in Fig. 3 the kink widths l_1 and l_2 do not necessarily have to be equal. This sets our work apart from other studies where it is commonly assumed that they are the same [30,38]. The energies of the kink-pair configurations shown in the figure need to be computed piecewise, adding the contributions from all the dislocation segments. In the next sections we provide expressions for each of the energy terms introduced in Eq. (2).

1. The mechanical work

The mechanical work W_m in Eq. (2) is simply defined as:

$$W_m(\tau, \{\boldsymbol{r}_i\}) = \tau b A \tag{3}$$

where τ, b, and A are, respectively, the resolved stress on the glide plane, the magnitude of the Burgers vector, and the area swept by the kink pair. This area can be calculated as:

$$A = \tfrac{1}{2}(|\boldsymbol{AB} \times \boldsymbol{AC}| + |\boldsymbol{DC} \times \boldsymbol{DA}|). \tag{4}$$

2. Self-energies of dislocation segments

In accordance with Hirth and Lothe [36] and Koizumi *et al.* [38], the total elastic self-energy of the configuration in Fig. 3 can be written as:

$$\Delta E^{\text{el}}_{\text{self}}(\{\boldsymbol{r}_i\}) = E^{\text{el}}_{\text{self}}(\boldsymbol{AB}) + E^{\text{el}}_{\text{self}}(\boldsymbol{BC}) + E^{\text{el}}_{\text{self}}(\boldsymbol{CD}) - E^{\text{el}}_{\text{self}}(\boldsymbol{AD}). \tag{5}$$

Here we use the nonsingular expressions for the self-energy of a straight dislocation segment $\boldsymbol{m}$ defined by endpoints $\boldsymbol{r}_1$ and $\boldsymbol{r}_2$, and Burgers vector $\boldsymbol{b}$ provided by Cai *et al.* [53], which give these energies as a function of θ and a. In this work, we add the core energy contribution to the above elastic energies as:

$$E_{\text{self}}(\boldsymbol{m}) = E^{\text{el}}_{\text{self}}(\boldsymbol{m}) + e_c(\theta, a)\|\boldsymbol{m}\|. \tag{6}$$

3. Interaction energies

For the interaction energies, Hirth and Lothe [36] give the following expression for a symmetric kink pair.

$$\Delta E_{\text{int}}(\{\boldsymbol{r}_i\}) = 2[E_{\text{int}}(\boldsymbol{LA}/\boldsymbol{AB}) + E_{\text{int}}(\boldsymbol{LA}/\boldsymbol{BC}) + E_{\text{int}}(\boldsymbol{LA}/\boldsymbol{CD}) + E_{\text{int}}(\boldsymbol{AB}/\boldsymbol{BC}) - E_{\text{int}}(\boldsymbol{LA}/\boldsymbol{AD})] + E_{\text{int}}(\boldsymbol{AB}/\boldsymbol{CD}) \tag{7}$$

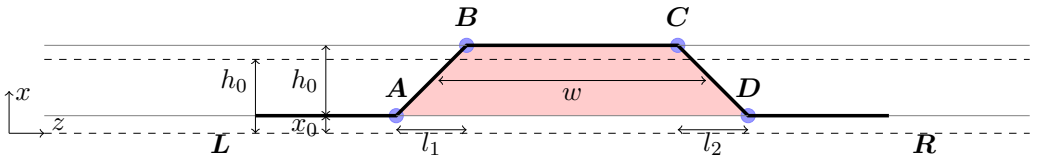

FIG. 3. Schematic representation of a kink-pair configuration on a straight screw dislocation. The points labeled $\boldsymbol{L}$ and $\boldsymbol{R}$ represent arbitrarily distant locations to the left and right of $\boldsymbol{A}$ and $\boldsymbol{D}$, respectively. We use a cartesian coordinate system such that the x direction is along the glide direction, the y direction is normal to the glide plane, and z is oriented along the line. x_0 is the equilibrium position of a straight screw segment at a finite stress τ, defined in equation (12). h_0 is the periodicity of the Peierls potential, w is the distance between kinks, and l_1 and l_2 are the widths of the kinks (projections of the $\boldsymbol{AB}$ and $\boldsymbol{CD}$ segments on x). The shaded region corresponds to the slipped area defined in Eq. (4).

where, by symmetry, the following equivalences can be established:

$$E_{\text{int}}(\boldsymbol{LA}/\boldsymbol{AB}) \equiv E_{\text{int}}(\boldsymbol{DR}/\boldsymbol{CD})$$
$$E_{\text{int}}(\boldsymbol{LA}/\boldsymbol{BC}) \equiv E_{\text{int}}(\boldsymbol{DR}/\boldsymbol{BC})$$
$$E_{\text{int}}(\boldsymbol{LA}/\boldsymbol{CD}) \equiv E_{\text{int}}(\boldsymbol{DR}/\boldsymbol{AB})$$
$$E_{\text{int}}(\boldsymbol{AB}/\boldsymbol{BC}) \equiv E_{\text{int}}(\boldsymbol{CD}/\boldsymbol{BC})$$
$$E_{\text{int}}(\boldsymbol{LA}/\boldsymbol{AD}) \equiv E_{\text{int}}(\boldsymbol{DR}/\boldsymbol{AD}).$$

However, for an asymmetric configuration, only the last one is true and, thus, the sum of interaction energies reads:

$$\begin{aligned}\Delta E_{\text{int}}(\{\boldsymbol{r}_i\}) = {} & E_{\text{int}}(\boldsymbol{LA}/\boldsymbol{AB}) + E_{\text{int}}(\boldsymbol{DR}/\boldsymbol{CD}) + E_{\text{int}}(\boldsymbol{LA}/\boldsymbol{BC}) \\ & + E_{\text{int}}(\boldsymbol{DR}/\boldsymbol{BC}) + E_{\text{int}}(\boldsymbol{LA}/\boldsymbol{CD}) \\ & + E_{\text{int}}(\boldsymbol{DR}/\boldsymbol{AB}) + E_{\text{int}}(\boldsymbol{AB}/\boldsymbol{BC}) + E_{\text{int}}(\boldsymbol{CD}/\boldsymbol{BC}) \\ & - 2E_{\text{int}}(\boldsymbol{LA}/\boldsymbol{AD}) + E_{\text{int}}(\boldsymbol{AB}/\boldsymbol{CD}). \end{aligned} \tag{8}$$

The general expression within nonsingular isotropic elasticity theory for the interaction energy of two segments $\boldsymbol{m}$ and $\boldsymbol{n}$ with, respectively, endpoints $\boldsymbol{r}_1$ and $\boldsymbol{r}_2$, and $\boldsymbol{r}_3$ and $\boldsymbol{r}_4$ is:

$$\begin{aligned} E_{\text{int}}(\boldsymbol{m},\boldsymbol{n}) = {} & E^*(\boldsymbol{r}_4 - \boldsymbol{r}_2) + E^*(\boldsymbol{r}_3 - \boldsymbol{r}_1) \\ & - E^*(\boldsymbol{r}_4 - \boldsymbol{r}_1) - E^*(\boldsymbol{r}_3 - \boldsymbol{r}_2) \end{aligned} \tag{9}$$

where the functional E^* takes different forms depending on the nature of the interaction. The nonsingular elastic expressions used here to obtain E^* are all given by Cai *et al.* [53], which we include in Appendix C, in case they could be valuable for the reader.

4. The Peierls potential

The kink pair structure shown in Fig. 3 rests on a periodic energy landscape known as the Peierls potential, U_{P}. Multiple atomistic studies using DFT and semiempirical potentials [28,54,55] have shown that U_{P} is well represented by a (co)sinusoidal function of the type:

$$U_{\text{P}}(x) = \frac{U_0}{2(1-\alpha)}\left[1 - \cos\frac{2\pi x}{h_0} - \frac{\alpha}{2}\left(1 - \cos\frac{2\pi x}{h_0}\right)^2\right] \tag{10}$$

where x represents the reaction coordinate (along the glide direction), U_0 is known as the Peierls energy, and h_0 is the period of U_{P} ($h_0 = a_0\sqrt{6}/3$ in bcc lattices). α is a parameter that captures the deviation of U_{P} from a pure cosine function. The contribution to the total energy of a kink segment lying across two Peierls valleys is:

$$\Delta U_{\text{P}}(\{\boldsymbol{r}_i\}) = \int_{\boldsymbol{LABCDR}} U_{\text{P}}(x)d\ell - \int_{\boldsymbol{LADR}} U_{\text{P}}(x)d\ell. \tag{11}$$

Both of the above integrals are evaluated from an equilibrium position x_0 to $x_0 + h_0$. x_0 is obtained from the following relation:

$$\left.\frac{dU_{\text{P}}(x)}{dx}\right|_{x=x_0} = \tau b. \tag{12}$$

The infinitesimal differential $d\ell$ follows along the kink segment and can be linearized as:

$$d\ell = \sqrt{dx^2 + dz^2}.$$

We now make the approximation that the straight segments $\boldsymbol{LA}$, $\boldsymbol{BC}$, $\boldsymbol{DR}$ cancel with their respective counterparts in the $\boldsymbol{LADR}$ configuration. Then the above integrals reduce to:

$$\Delta U_{\text{P}}(\{\boldsymbol{r}_i\}) = \int_{x_0}^{x_0+h_0} U_{\text{P}}(x)(d\ell_1 + d\ell_2) - U_{\text{P}}(x_0)(l_1 + l_2). \tag{13}$$

To capture the effect of the resolved shear stress on the shape of $U_{\text{P}}(x)$ revealed in Sec. II A, we consider a stress dependence of both $U_0(\tau)$ and $\alpha(\tau)$, as will be shown in Appendix A.

Equations (3), (5), (8), and (13) are combined to fully define the activation enthalpy in Eq. (2), which is subsequently optimized for the set of parameters w, l_1, and l_2 as a function of stress. Each saddle point corresponds to the activated state of the kink pair at each stress, from which the dependence of $\Delta H(w, l_1, l_2)$ with τ can be calculated. The dimensions of the trapezoid corresponding to each optimized configuration are obtained as:

$$\boldsymbol{r}_A \equiv (x_0, 0)$$
$$\boldsymbol{r}_B \equiv (x_0 + h_0, l_1)$$
$$\boldsymbol{r}_C \equiv (x_0 + h_0, l_1 + w)$$
$$\boldsymbol{r}_D \equiv (x_0, l_1 + w + l_2).$$

B. The line tension model as a simplified LOS approach

At low stresses the stability of the kink-pair configuration is controlled by the elastic interaction between the kink segments. However, as the stress increases and the shape of the line resembles more a 'bulged' structure with low curvature. In such cases, the elastic energy of the system is well approximated by a so-called *line tension* representation [56,57], where the energy of the kink-pair structure is controlled by the curvature of nonstraight segments. Within elasticity, the line tension is defined as:

$$T(\theta, a) = \frac{\partial E_{\text{self}}(\theta, a)}{\partial \ell} \tag{14}$$

which is the dislocation energy per unit length, depending only on dislocation character θ and the core width a. For small dislocation segment lengths ℓ, the above expression can be approximated by $T(\theta, a) \approx \frac{E_{\text{self}}(\theta,a)}{\ell}$. This form of $T(\theta, a)$ replaces the self and interaction elastic energies in the enthalpy expression for the kink-pair configuration. $\Delta H(\{\boldsymbol{r}_i\})$ now reads:

$$\begin{aligned}\Delta H(z, \tau) = {} & \int dz[\Delta T(\theta(z), a) + \Delta e_c(\theta(z), a) \\ & + \Delta U_{\text{P}}(x(z), \tau) - W_m(\tau)] \end{aligned} \tag{15}$$

$$\begin{aligned} = {} & \int dz[(T(\theta(z), a) - T(\theta = 0, a)) \\ & + (e_c(\theta(z), a) - e_c(\theta = 0, a)) \\ & + \Delta U_{\text{P}}(x(z), \tau) - W_m(\tau)] \end{aligned} \tag{16}$$

where e_c, W_m, and ΔU_{P} are defined as in Secs. II B, III A 1, and III A 4. Equation (15) can be represented as a piecewise sum along the z direction of the contributions of individual

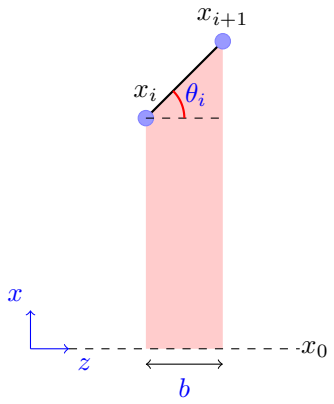

FIG. 4. Representation of a discrete segment used to calculate the enthalpy of the kink-pair configuration using the line tension LOS model. x_0 is calculated as in Eq. (12).

segments of length b [39]:

$$\Delta H(\{x_i\},\tau) = b\sum_i \Big[T(\theta_i,a) - T(\theta=0,a) + (e_c(\theta_i,a) - e_c(\theta=0,a)) + \Delta U_{\rm P}(x_i,\tau) - \frac{\tau b}{2}(x_{i+1}+x_i-2x_0)\Big] \tag{17}$$

where $U_{\rm P}(x,\tau)$ is given by equation (10), and $\theta_i = \tan^{-1}\left(\frac{x_{i+1}-x_i}{b}\right)$. The geometry of one discretization segment is shown in Fig. 4 for the calculation of the mechanical work.

The expression utilized in Eq. (14) is derived from those provided by Cai *et al.* [53], which expressed in piecewise form for use in Eq. (17) is:

$$T(\theta,a) = \frac{\mu b^2}{4\pi(1-\nu)}\left\{(1-\nu\cos^2\theta)\ln\frac{b+\sqrt{b^2+a^2}}{a} - \frac{3-\nu}{2}\left(\frac{\sqrt{b^2+a^2}-a}{b}\right)\cos^2\theta\right\}. \tag{18}$$

The equilibrium configurations are obtained by minimizing the value of ΔH in Eq. (17) as a function of the set of coordinates $\{x_i\}$ at each stress point τ.

IV. IMPLEMENTATION AND PARAMETRIZATION OF LOS MODELS

In this section we explain how to process the atomistic results described in Sec. II for use in the EI and LT models just presented. First, we discuss the expressions for the stress dependence of the Peierls potential, followed by those pertaining to the core energies.

A. The Peierls potential

For the EI model, the integral in Eq. (13) can be solved analytically and used directly in expression (2):

$$\begin{aligned}\Delta U_{\rm P}(\{\boldsymbol{r}_i\}) &= \left(\sqrt{1+\frac{l_1^2}{h_0^2}}+\sqrt{1+\frac{l_2^2}{h_0^2}}\right)\int_{x_0}^{x_0+h_0} U_{\rm P}(x)dx - U_{\rm P}(x_0)(l_1+l_2)\\ &= \frac{U_0}{2(1-\alpha)}\left\{\left(\sqrt{1+\frac{l_1^2}{h_0^2}}+\sqrt{1+\frac{l_2^2}{h_0^2}}\right)\left[h_0\left(1-\frac{3\alpha}{4}\right) - \frac{h_0(1-\alpha)}{2\pi}\left(\sin\frac{2\pi(x_0+h_0)}{h_0} - \sin\frac{2\pi x_0}{h_0}\right)\right.\right.\\ &\quad\left.\left. - \frac{h_0\alpha}{16\pi}\left(\sin\frac{4\pi(x_0+h_0)}{h_0} - \sin\frac{4\pi x_0}{h_0}\right)\right] - (l_1+l_2)\left[1-\cos\frac{2\pi x}{h_0} - \frac{\alpha}{2}\left(1-\cos\frac{2\pi x}{h_0}\right)^2\right]\right\}\end{aligned} \tag{19}$$

where we have used $dz_\beta = \frac{l_\beta}{h_0}dx$, with $\beta = 1, 2$. The atomistic information provided in Sec. II A has been introduced into this expression in the form of stress-dependent correlations for U_0 and α. We have seen that U_0 scales as τ^n whereas α is a linear function of τ. The specific expressions and the fitting procedure followed to obtain these correlations is described in Appendix A.

For the LT model, $U_{\rm P}(x_i)$ is evaluated directly using (10) for each discretized segment x_i. Summation over all segments then gives us the total potential energy of the line, in accordance with Eq. (17). The expressions for $U_0(\tau)$ and $\alpha(\tau)$ are identical to those used in the EI model.

B. Core energies

The core energy results from atomistic calculations shown in Sec. II B are introduced in the same manner in the EI and LT models. In principle, the main features of e_c that a fitting procedure must capture are its dependence of both dislocation character (i.e., angle θ) and core width a. However, what is different in this work is the slight asymmetry about the edge character orientation displayed in Fig. 2. For this, we additively separate the total core energy into an a-independent term and an a-dependent one:

$$e_c(\theta,a) = f(\theta) + g(\theta)\log\left(\frac{a}{b}\right) \tag{20}$$

where $f(\theta)$ and $g(\theta)$ are obtained by fitting the data in Fig. 2 to Fourier series expansions of the type:

$$y(\theta) = c_0 + \sum_{k=1}^{3} c_k\sin(2k\theta) + d_k\cos(2k\theta). \tag{21}$$

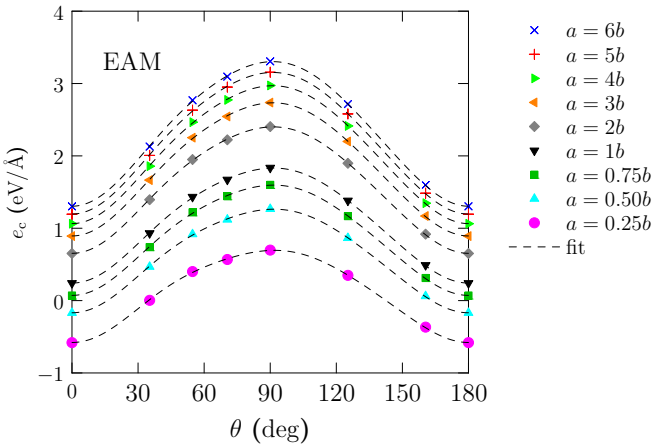

FIG. 5. Dislocation core energies for EAM interatomic potentials as a function of the dislocation character angle θ and the core size a. The curves generated using Eq. (20) for nine different values of a are also plotted.

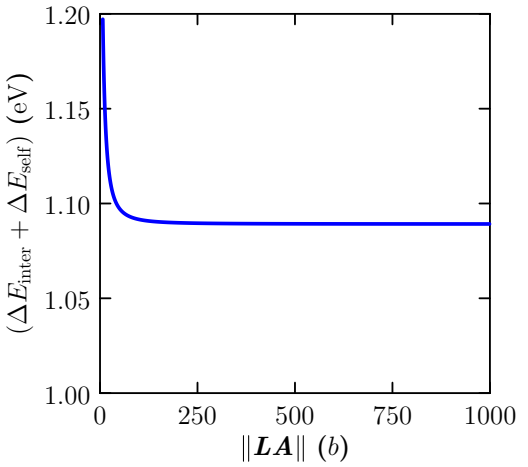

FIG. 6. Elastic interaction and self energies as a function of the length of ***LA*** and ***DR*** segments.

These functions can yield the asymmetry about $\theta = \pi/2$ and naturally satisfy the condition that their first derivative is equal to zero for $\theta = 0$ and $\theta = \pi$ (zero self-force for screw orientation). It is important to clarify that this partition of the core energy is mathematically arbitrary, and other works have opted for different approaches [58]. The dependence of the dislocation core energy with both the character angle and the core size is shown in Fig. 5. The details about the fitting procedure and the numerical values of the coefficients c_k and d_k are given in Appendix B.

C. Implementation details

1. Elastic interaction model

In the EI model, the kink-pair configuration itself represents the activated state between the two minima in the Peierls potential representing the initial and final screw dislocation configurations. As such, the enthalpy in Eq. (2) must be maximized along the reaction path. This is done by obtaining the saddle point of the entire structure as a function of the position of points ***A***, ***B***, ***C***, and ***D*** in Fig. 3. However, standard (unconstrained) optimization algorithms are difficult to stabilize in an energy landscape that is only conditionally convergent [59]. The geometry of the configuration, however, can be used to identify conditions that favor convergence.

This can be done, for example, by noting that the trapezoid depicted in Fig. 3 represents a dislocation loop (with three 'real' segments and one 'anti' segment) whose elastic energy is known to be finite. This imposes limits on the minimum and maximum size of the trapezoidal structure that are discussed below.

(i) The condition of finite energy means that the total activation enthalpy in Eq. (2) is independent of the size of segments ***LA*** and ***DR***. Using isotropic singular linear elasticity, the terms depending on the lengths of these segments are seen to cancel in the analytical expressions for the total elastic energy of the trapezoidal configuration. With the nonsingular theory, things are not quite as simple, as analytical expressions are not straightforward to obtain. However, the same premise must still hold. Here, we have performed a numerical study to confirm this and have established the minimum length of segments ***LA*** and ***DR*** to have converged, length-independent energies. Figure 6 shows the combined value of $(\Delta E_{\text{int}} + \Delta E_{\text{self}})$ in Eq. (2) as a function of the value of $\|\boldsymbol{LA}\| \equiv \|\boldsymbol{RD}\|$. Our results show that values of approximately $200b$ or larger must be used to achieve length independence. In most simulations, we have typically used a value of $1000b$.

(ii) At the same time, the separation of segments ***AB*** and ***CD*** (i.e., the value of w in Fig. 3) must be sufficiently small for the elastic interaction energy to be finite within the numerical tolerance of our minimization procedure. w changes with stress, but we have found that, as a rule of thumb, at zero stress, values of no less than $40b$ should be considered.

2. Line tension model

The case of the LT model differs from that of the EI model just explained. In this case, the saddle point configuration corresponds to a bulged structure that lies somewhere along the x coordinate. This configuration does not generally correspond to one where the line lies on either of the minima of U_{P}. Therefore, one must vary the size of the bulge, defined by a variable h along the x path between x_0 and h_0 until the system's enthalpy goes through a maximum. At each stress, this path is discretized and the saddle point structure found. This is expected to yield minimum energy paths that are substantially equivalent to dynamic trajectories [60]. To improve the rate of convergence, here we invert the potential energy landscape by altering the sign of the mechanical work along the path as to balance the rest of the terms in the enthalpy and have net zero effect on the total energy. This approach has proven robust for the calculations undertaken in this work.

Once the saddle-point configuration is found for each stress, we approximate the left and right sides of the bulged structure with an arc tangent function. All the corresponding outputs (i.e., w, l_1, l_2, etc.) are calculated upon mathematical analysis of the best approximants obtained for each case.

TABLE I. Interatomic potential-specific parameters. The top half of the table includes atomistic parameters used in the LOS models: a_0 is the lattice constant, τ_P is the Peierls stress, U_{lk} and U_{rk} are the energies of left and right kinks, respectively, and $\Delta H_0 = U_{lk} + U_{rk}$ is the zero-stress kink-pair activation enthalpy. The bottom half of the table lists values of parameters extracted from the LOS model calculations, separated between EI and LT calculations: a is the core width, p and q are the exponents of the phenomenological kink-pair enthalpy expressions, ΔH_0^* is the intercept of the kink-pair activation enthalpy with the vertical axis, and τ_a is the stress at which the activation enthalpy vanishes, equivalent to the *athermal* stress in experimental tests.

	EAM		MEAM	
a_0 [Å]	3.19		3.14	
τ_P [GPa]	2.0		3.4	
U_{lk} [eV]	0.71		0.81	
U_{rk} [eV]	0.92		0.99	
ΔH_0 [eV]	1.63		1.80	
	EI	LT	EI	LT
a [b]	0.70	0.80	0.15	0.50
p	0.41	0.83	0.45	0.80
q	1.05	1.38	1.09	1.46
ΔH_0^* [eV]		1.68		1.84
τ_a [GPa]	1.84	1.99	3.22	3.61

V. RESULTS

The first-principles method used here for parametrizing and benchmarking the LOS model calculations are atomistic calculation results using two different interatomic potentials, EAM and MEAM. All atomistic calculations were done using molecular statics at 0 K. Table I (top half) gives several parameters of importance obtained for each potential. Below, we discuss the most important results for the EI and LT models. Most results are shown in normalized form to facilitate intercomparison: (i) the stress is expressed as the fraction of the Peierls stress, $s = \tau/\tau_P$, (ii) energies are plotted relative to the zero-stress activation enthalpy ΔH_0, and (iii) lengths are expressed in Burgers vector units b or Peierls potential wavelength h_0.

A. System length scales: Line shapes, kink separation, and kink widths

For the sake of clarity, we only show results for the EAM potential in the main body of the text and discuss MEAM results in the context of each EAM graph (more discussion provided in Sec. VI and Appendix D).

Figure 7 shows the optimized saddle point configurations for kink pairs as a function of stress under the EI and LT models for the EAM potential (the configurations obtained using the MEAM potential are qualitatively similar to those obtained using the EAM potential). The graphs for the EI model results do not show segments ***LA*** and ***DR*** in their entirety but a diminishing kink separation w can generally be observed as the stress increases. This variation of w with τ is plotted in Fig. 8. In accordance with elasticity theory, the kink-pair length diverges at zero stress, decreasing gradually with stress to a final value of $\approx 2b$. For its part, lacking an interaction energy, the results for w in the LT model are less significant, but they are weakly dependent on stress. Interestingly, LT predictions for the EAM and MEAM potentials result in differences of about a factor of two between both atomic models (higher for MEAM). As well, EAM values are in very good agreement with the corresponding atomistic results (around $10b$, from Ref. [41]).

As shown in Fig. 7 for the LT model, the activated state for the dislocation is a bulged configuration straddling the Peierls potential. The amplitude of this bulge is plotted in Fig. 9 as a function of stress for the EAM potential. As the figure indicates, this amplitude coincides with the wavelength of $U_P(x)$, h_0 at zero stress, and is zero at the Peierls stress, consistent with the definition of the activated state at both ends of the stress range. Our results show excellent agreement with the expected analytical form for h in line tension models [60,61] (shown as lines in Fig. 9).

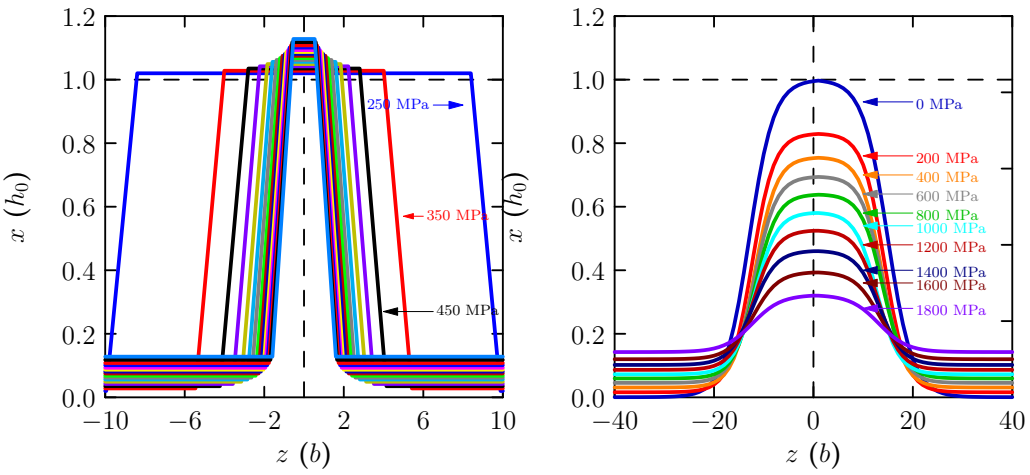

FIG. 7. Optimized kink pair configurations as a function of stress for the EAM potential. (a) Elastic interaction model. (b) Line tension model.

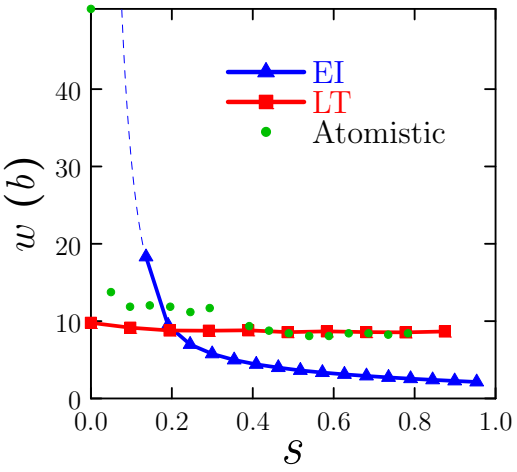

FIG. 8. Kink separation in the kink pair under stress (normalized to the corresponding Peierls stress). The EI results indicate divergence at zero stress, in accordance with elasticity theory, while the LT values are finite at all stresses. Atomistic results for the EAM potential are shown for comparison, showing very good agreement with predictions by the LT model.

While these results are interesting, one of the most important aspects in this work is the asymmetry in the dislocation core energies introduced in Sec. II B. This asymmetry manifests itself as differing kink 'widths', i.e., the spreading length along the dislocation line (z coordinate) of the segments connecting two consecutive Peierls valleys. These are labeled l_1 and l_2 in Fig. 3.

The results for these two lengths are shown in Fig. 10. With the EI model, there are slight differences between the left and right kinks, with the left one l_1 being larger than the right one l_2. Contrary to the situation of the kink-pair separation w, here the EAM kinks spread over approximately twice the distance of the MEAM ones. These results also show a slow decrease of l_1 and l_2 with stress (kinks approaching the edge orientation), although interestingly these widths are around

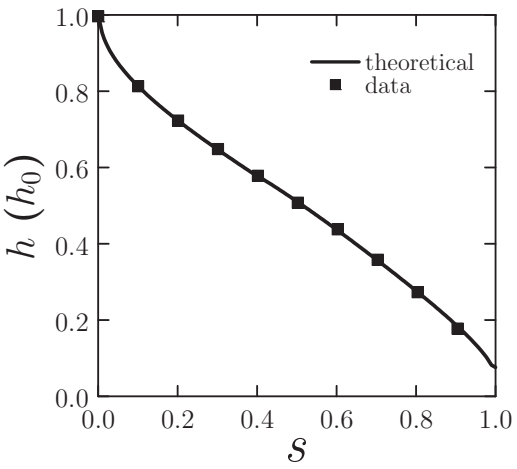

FIG. 9. Amplitude of the saddle-point configuration for the LT model as a function of stress. The results for EAM (black squares) agree well with theoretical predictions [61] (solid line).

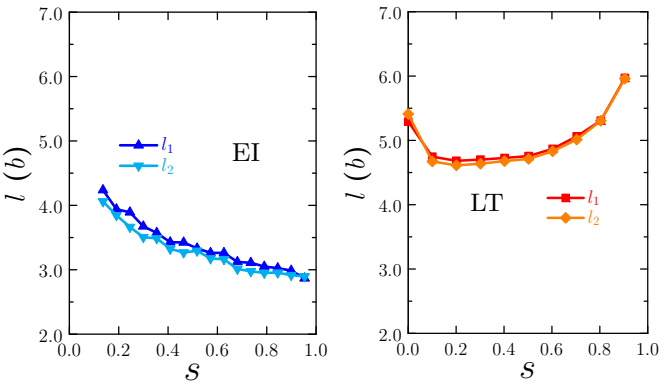

FIG. 10. Kink widths, l_1 and l_2 (refer to Fig. 3), as a function of stress.

1.5b for the MEAM potential and between 3 and 4b for EAM. This stands in contrast to atomistic results, which predict kink widths of approximately 25b for EAM calculations [41]. For their part, LT results show no appreciable difference between l_1 and l_2. Here too calculations for the EAM potential result in larger kink widths than for the MEAM potential, between 4.5 and 6b vs 3 and 4b, respectively. However, l_1 and l_2 display a different dependence with stress in this case, reaching a minimum at low stresses but growing with stress subsequently.

B. System energies: Kink energies and activation enthalpies

The most important physical quantity to extract from our models is the kink-pair activation enthalpy as a function of stress. This is used in a number of approaches to describe thermally-activated screw dislocation motion in bcc metals (as it has been done in our works in the past, e.g., Refs. [41,62]). In Fig. 11 we show the results for the EI and LT models. To facilitate comparison, we normalize the enthalpies by the unstressed activation enthalpy obtained in atomistic calculations in each case, ΔH_0, and the stresses by the Peierls stress τ_P. These parameters are all given in Table I. Note that (i)

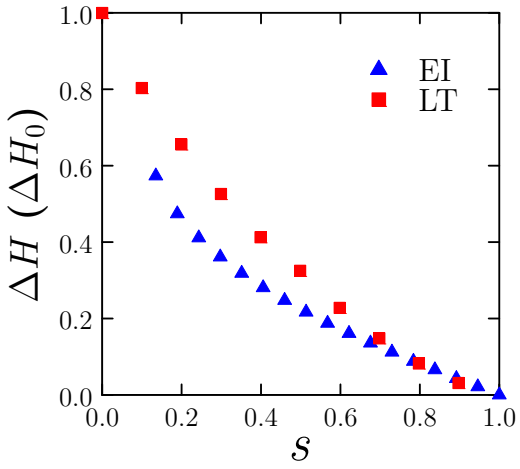

FIG. 11. Kink-pair activation enthalpy for the EI and LT models. The results are normalized to the unstressed activation enthalpy obtained in atomistic calculations and the Peierls stress in each case (refer to Table I).

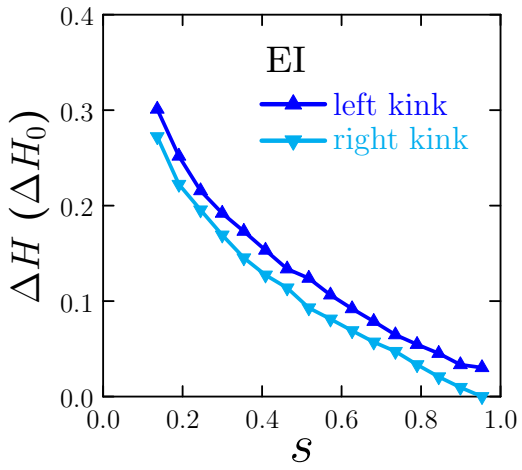

FIG. 12. Energies of individual kinks for LT models for EAM potential. The differences are due to the asymmetry of the core energy functions about the edge orientation.

the enthalpy at zero stress for the EI model is undefined and therefore the data point shown in Fig. 11 is the atomistic value, and (ii) that the actual intercept of the activation enthalpy curves for the LT model with the vertical axis does not necessarily correspond to the atomistic value.[2] This is what is labeled as ΔH_0^* in Table I. Similarly, intercepts with the stress axis in all cases do not necessarily match the value of τ_P, with the actual values labeled as τ_a in Table I. We interpret these stresses as being the 'athermal' limits for the kink-pair mechanism in each case.

Most importantly, the values of a used in Eqs. (6), (8), and (18) to obtain these energies have been chosen as to provide the best fit of the activation enthalpy curves to the known atomistic values of ΔH_0 and τ_P. In other words, we arbitrarily set the core width value to match known 'first-principles' calculations of the potential in question. These values of a are provided also in Table I and, as can be seen, are always less than one Burgers vector distance. We will return to this issue in Sec. VI.

Finally, it is common practice to fit the curves in Fig. 11 to the Kocks-Ashby-Argon phenomenological expression [63]:

$$\Delta H(\tau) = \Delta H_0 \left(1 - \left(\frac{\tau}{\tau_P}\right)^p\right)^q, \tag{22}$$

where p and q are exponents that describe the asymptotic behavior of $\Delta H(\tau)$ in the limits of zero stress ($q = 1.25$) and the Peierls stress ($p = 0.5$) for isotropic linear elasticity [57]. Since tungsten is elastically isotropic, our model provides an excellent testbed for these values, which have indeed been reproduced for stress-independent U_P and symmetric $e_c(\theta, a)$. These exponents are also provided in Table I. Note that we use Eq. (22) only to facilitate comparison across the atomistic, EI, and LT model results (and for the EAM and MEAM cases) via the values of p and q, without implying its validity for any specific case.

[2]It is also important to note that ΔH_0 is obtained atomistically via procedures that are insensitive to periodic image interactions [40].

To evaluate again the effect of the core energy asymmetries on the energetics of the activated states, we calculate in Fig. 12 the individual kink energies as a function of τ. As no appreciable difference was found for the LT model predictions, we omit them from the figure for clarity. The energies shown include the interaction and self-energies in the EI model of the kink segments only. Only a noticeable difference can be found for the EAM results, approximately 10%, whereas kinks energies are practically identical for the MEAM potential. The individual atomistic kink energies are given in the table above as well (for zero stress), differing about 20% between themselves. We also discuss this more in depth in the next section.

VI. DISCUSSION

A. Comparisons between LOS models

As indicated in Sec. I, different approximations to the line integral along the x (glide) direction to calculate the energy of the activated kink-pair state result in different LOS model formulations, each with its own advantages and disadvantages. The EI model approximates the bulge configuration better at low stresses, when the activated state extends across the entire Peierls potential period and the kink-pair energy is dominated by elastic interactions between kink segments. This allows the use of a simple trapezoidal structure to represent the system, which has the benefit of consisting of only four degrees of freedom. This considerably speeds up convergence of the energy minimizations, which allows us to study the parametric space of the model efficiently. The aspect of the EI model used here is the asymmetry of the left and right kinks, by virtue of the character dependence of the core energy function. Regarding this, the EI model results predict differences of less than 1% in the kink widths for both EAM and MEAM parameters (Fig. 10), while the difference in enthalpy is slightly larger (Fig. 12).

For its part, the LT model is best suited for lines with small curvature, when the bulge configuration is small, a situation typically encountered at high stresses. The implementation of the LT approach involves, however, up to hundreds of discrete segments, which increases the computational time severalfold compared to the EI model. LT results show no discernible difference in the values of both the energies and the kink widths. Thus, it appears that the LT model is less sensitive to the core energy asymmetry than the EI model.

In terms of EAM vs MEAM differences, as shown in Fig. 11, when normalized to the corresponding values of ΔH_0 and τ_P, the shapes of the LT and EI models differ in less than 3%. This is an encouraging result as it could potentially indicate that normalized LOS model predictions can be transferred across different potentials, which would eliminate a common source of variability in dislocation property calculations.

B. Defining the core size by matching LOS models to atomistic data

The size of the dislocation core (a in this work) is a mathematical construct introduced to remove the singularity inherent to the theory of elasticity. As such, it does not possess

any intrinsic physical meaning, serving instead as an arbitrary limit between the elastic and inelastic regions. However, one can remove some of this arbitrariness by matching the LOS model calculations to atomistic results of the total energy of kink pair configurations. By adjusting the value of a to partition the elastic and core energies in Eqs. (1) and (20) in such a way as to match the atomistic kink-pair energies at zero stress (obtained independently for the EAM and MEAM potentials), one can relate the value of the core width to the size of a region that contains the inelastic contribution to the total energy. Following this approach, we obtain values of $0.7b$ (EI) and $0.8b$ (LT) for the EAM case ($\Delta H_0 = 1.63$ eV) and $0.2b$ and $0.5b$ for MEAM ($\Delta H_0 = 1.78$ eV). The fact that these are between half and a full Burgers vector may be indicative of the order of magnitude to be expected for this parameter. However, we emphasize that this is one attempt to establish the value of a using a physical criterion, but it is difficult to ascertain how accurate or valid it is relative to other approaches [64–66]. In any case, we believe this to be an interesting aspect of our calculations and worth reporting as an original application of LOS models.

C. Building 3D kink-pair models from 2D atomistic data

One of the advantages of studying straight dislocations is the existence of translational symmetry along the line direction, which generally reduces the study of its properties to quasi-2D structures that need only capture the minimum repeatable translational unit along the dislocation line. For screw dislocations, this length is of course the Burger's vector, which is typically the shortest lattice vector of the crystal. For this reason, general dislocation properties can be efficiently and accurately calculated using thin atomistic supercells, which makes them amenable to electronic structure calculations. The existence of kink pairs breaks the translational symmetry of screw dislocations in bcc (and other) crystals. Being the fundamental structure governing screw dislocation dynamics, this necessitates using 3D configurations which precludes the use of computationally demanding approaches such as DFT. Consequently, it has been a goal of the bcc plasticity community to assess whether 2D information such as what has been presented here (Secs. V A and V B) suffices to capture 3D behavior when incorporated into efficient continuum models of dislocation line configurations.

Our calculations provide a testbed for this idea, in line with prior efforts [55], as they allow a direct comparison to strictly atomistic results of kink-pair configurations using EAM [41,62]. This is illustrated in Fig. 13, where a good agreement between the LOS results and the atomistic calculations can be appreciated. As the figure shows, the LT model agrees with the atomistic result at low stresses, while the EI model produces a better match at high stresses. While this may appear contradictory with the common assumption that the EI is better suited for low stresses and the LT model for high stresses, the nonscrew segments of the trapezoid in the EI case are highly tilted towards the screw character due to the combined action of dislocation self and core energies,which is not unusual in bcc metals. This makes the standard assumption of the EI model weakly true in this case. For its part, the LT model works well at low stresses not due to the shape of the kinks but because it provides stable kink-pair configurations at stresses where elastic models do not converge. Partially, this is because dislocation segments do not interact with one another in the LT framework, the driving force is only the curvature of the line, which is always minimized for a given applied stress. At high stresses, the LT fails because the line is 'bulged', i.e., it has so much curvature that the noninteraction assumption starts to fail. In the intermediate stress range, the EAM calculations lie in between both LOS approaches. Albeit restricted to very specific conditions, this verification result suggests that continuum models parameterized with atomistic 2D results can indeed be good approximants of full atomistic behavior in tungsten. While it is not clear how much of this agreement can be attributed to specific features of W, such as elastic isotropy or the choice of interatomic potential, we can cautiously conclude that LOS models that employ 2D information can be trusted to provide acceptable estimates of ΔH in other bcc metals.

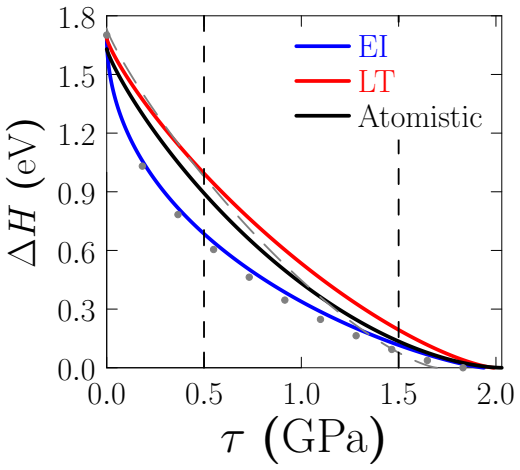

FIG. 13. Comparison of EI, LT, and atomistic models for the EAM potential fitted to Eq. (22). The gray dashed line corresponds to LT results assuming no asymmetry in the core energies and no stress dependence of the Peierls potential ($p = 0.88$, $q = 1.37$), while the gray dotted line is the equivalent EI curve ($p = 0.50$, $q = 1.29$). The vertical dashed lines indicate the limits of the 'low' and 'high' stress regions, defined *ad hoc* to be at $0.25\sigma_{\rm P}$ and $0.75\sigma_{\rm P}$, respectively.

D. Discussion of other works

Researchers have been calculating kink-pair activation enthalpies using continuum elastic models since the 1950s. As atomistic information involving fundamental dislocation properties has become available [28,58], we have been able to enrich continuum formulations and increase their physical accuracy. There are several examples of this in the literature [39,52,55,66], each highlighting one specific aspect of the physics of kink pairs in screw dislocations in bcc metals. However, this work constitutes a LOS formulation to simultaneously integrate (i) the stress dependence of the Peierls potential, (ii) the asymmetry of the dislocation core energies with respect to dislocation character, and (iii) the extraction of the core width by matching LOS results with atomistic results.

VII. CONCLUSIONS

Our first conclusion is that one can successfully incorporate atomistic data obtained in quasi-2D conditions into continuum elastic models of 3D kink-pair configurations. We have demonstrated that the stress dependence of the Peierls potential and results for core energies as a function of dislocation character can be integrated into elastic interaction and line tension models in a straightforward manner. Moreover, we report a slight asymmetry in the core energies about the edge orientation in W, in accordance with a periodicity of $(0, \pi)$ for the dislocation character space in bcc metals.

The asymmetry in the dislocation core energies accounts for no more than 10% difference in left and right kink energies (compared to no less than 20% in atomistic results) and results in very slight variations in their spreading lengths. Thus, we conclude that, while they are likely one of several contributions to this energy asymmetry, core energies alone cannot capture it in its entirety. However, a representation of core energies in terms of the core width parameter is helpful to extract the value of this parameter by matching to atomistic data. In our particular case, we find that this core width is always less than one Burgers vector distance.

Including the stress dependence of the Peierls potential in the models appears to shift the athermal stresses to higher values compared to when just the zero stress potential is used, more in line with the atomistic values of the Peierls stress. However, this effect is small as well.

Finally, our results suggest that atomistic calculations of kink-pair configurations result in activation enthalpies that are in between elastic interaction and line tension predictions. In particular, at low stresses atomistic data agree better with line tension calculations, while at high stresses the agreement is better with full elastic models.

ACKNOWLEDGMENTS

The authors thank Dr. Emmanuel Clouet for fruitful discussions. D.C. acknowledges support from the Engineering HPC at Villanova University. S.H. and J.M. acknowledge support by the National Science Foundation under Grant No. DMR-1611342 and the U.S. Department of Energy's Office of Fusion Energy Sciences, Project DE-SC0012774:0001. Computer time allocations at UCLA's IDRE Hoffman2 supercomputer are acknowledged.

APPENDIX A: FITTING PROCEDURE OF THE STRESS DEPENDENCE OF THE PEIERLS POTENTIAL

Here we explain how to introduce the resolved shear-stress dependence in Eq. (10). The τ dependence enters through the parameters U_0 and α and our goal here then is to obtain compact expressions for $U_0(\tau)$ and $\alpha(\tau)$. To this end, we first plot the values of U_0 and α with stress in Figs. 14 and 15 for the EAM and MEAM potentials, respectively.

As the figures show, generally there is a nonlinear dependence of U_0 with stress and a linear one for α. Consequently, we use power laws for $U_0(\tau)$ and linear relationships for $\alpha(\tau)$.

(i) Fitting of U_0:

(a) EAM: Due to the change of convexity of the EAM U_0 data, we split the fitting into two regions.

(1) In the low stress region, $\tau \leqslant 0.8$ GPa,

$$U_0(\tau) = 0.005\tau^{1.49} + 0.06 \tag{A1}$$

(2) In the high stress region, $\tau > 0.8$ GPa,

$$U_0(\tau) = 0.21(\tau - 0.7643)^{0.005} - 0.14 \tag{A2}$$

(b) MEAM:

$$U_0(\tau) = 0.003(\tau - 0.13)^{1.6742} + 0.11 \tag{A3}$$

with U_0 expressed in [eV/b] when τ is expressed in GPa.

(ii) Fitting of α:

(a) EAM:

$$\alpha = 0.077\tau + 0.152 \tag{A4}$$

(b) MEAM:

$$\alpha = 0.115\tau - 0.515 \tag{A5}$$

with α nondimensional when τ is in GPa.

We emphasize that these expressions have no implied physical meaning and are simply used for convenience in the range of stresses considered here.

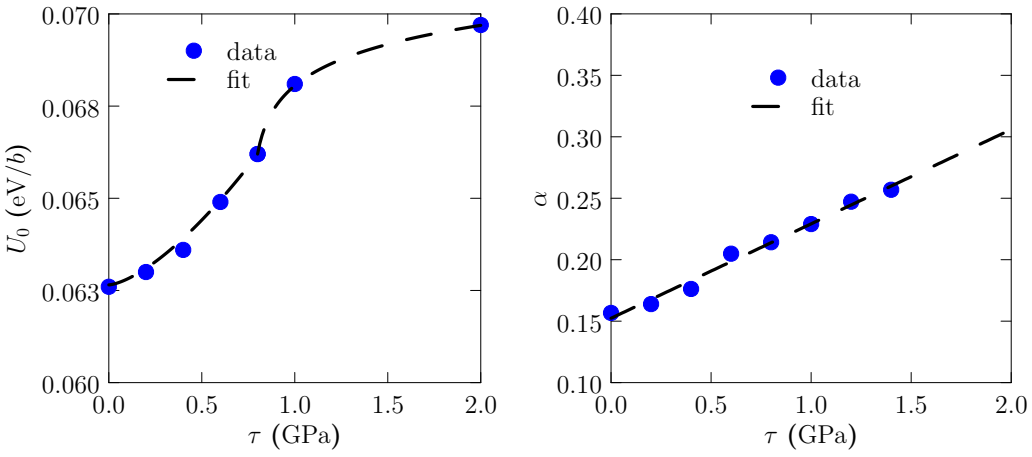

FIG. 14. Fitting of U_0 and α for the EAM potential.

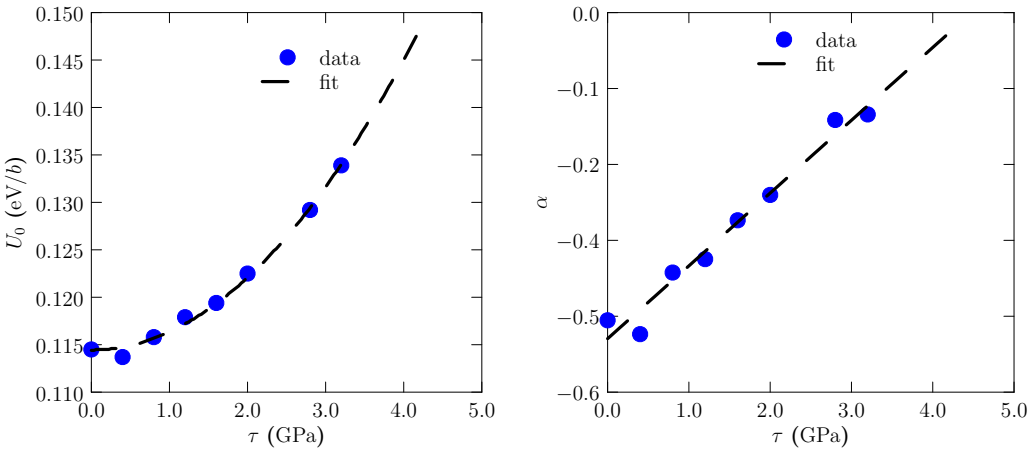

FIG. 15. Fitting of U_0 and α for the MEAM potential.

APPENDIX B: FITTING OF CORE ENERGY DATA

As it was shown in Sec. II B, dislocation core energies expressed as:

$$e_c(\theta, a) = f(\theta) + g(\theta)\log\left(\frac{a}{b}\right)$$

where both $f(\theta)$ and $g(\theta)$ are Fourier series of the type:

$$y(\theta) = c_0 + \sum_{k=1}^{3} c_k \sin(2i\theta) + d_k \cos(2i\theta).$$

Note that this form for $f(\theta)$ and $g(\theta)$ depends only on θ, with the a dependence contained exclusively in the logarithmic term. This mimics the partition represented by Eq. (1). The coefficients in these expressions are obtained by least-squares fitting to the atomistic data points obtained from Fig. 2 by varying a and θ, and are listed in Table II. $f(\theta)$ and $g(\theta)$ are plotted as a function of θ in Fig. 16 along with the corresponding Fourier series curves for the EAM and MEAM potentials.

APPENDIX C: EXPRESSIONS OF THE FUNCTIONAL E^* FOR THE INTERACTION ENERGIES

The functional E^* that appears in the formulation of the interaction energies E_{int} (cf. Sec. III) takes different forms depending on the nature of the interaction. In the following, the nonsingular elastic expressions given by Cai *et al.* [53] for parallel and nonparallel segments are provided. In both cases, the common Burgers vector to both segments is $\boldsymbol{b}$.

1. Nonparallel segments

This is relevant for the interaction between kink segments and screw segments. The energy functional $E^*(\boldsymbol{r}) \equiv E_{\text{np}}(\boldsymbol{r})$ is defined as:

$$\begin{aligned} E_{\text{np}}(\boldsymbol{r}) = \frac{\mu}{4\pi(1-\nu)(\boldsymbol{u}\cdot\boldsymbol{u})}\Bigg\{ & \boldsymbol{r}\cdot\ln\left[R_a + \boldsymbol{r}\cdot\boldsymbol{t}'\right]((A_1 \\ & - A_2')\boldsymbol{v}' + A_3'\boldsymbol{u}) + \boldsymbol{r}\cdot\ln[R_a + \boldsymbol{r}\cdot\boldsymbol{t}]((A_1 - A_2)\boldsymbol{v} \\ & + A_3\boldsymbol{u}) + A_4 R_a + \frac{(A_1 - A_5)[2(\boldsymbol{r}\cdot\boldsymbol{u})^2 + (\boldsymbol{u}\cdot\boldsymbol{u})a^2]}{\sqrt{(\boldsymbol{r}\cdot\boldsymbol{u})^2 + (\boldsymbol{u}\cdot\boldsymbol{u})a^2}} \\ & \times \arctan\left\{\frac{(1 + \boldsymbol{t}\cdot\boldsymbol{t}')R_a + \boldsymbol{r}(\boldsymbol{t} + \boldsymbol{t}')}{\sqrt{(\boldsymbol{r}\cdot\boldsymbol{u})^2 + (\boldsymbol{u}\cdot\boldsymbol{u})a^2}}\right\}\Bigg\} \end{aligned} \tag{C1}$$

where $\boldsymbol{t} = (\boldsymbol{r}_2 - \boldsymbol{r}_1)/L_m$ and $\boldsymbol{t}' = (\boldsymbol{r}_4 - \boldsymbol{r}_3)/L_n$ are the respective line tangents ($L_m = \|\boldsymbol{r}_2 - \boldsymbol{r}_1\|$ and $L_n = \|\boldsymbol{r}_4 - \boldsymbol{r}_3\|$), $\boldsymbol{u} = \boldsymbol{t} \times \boldsymbol{t}'$, $\boldsymbol{v} = \boldsymbol{u} \times \boldsymbol{t}$, $\boldsymbol{v}' = \boldsymbol{t}' \times \boldsymbol{u}$, and:

$$R_a = \sqrt{\boldsymbol{r}\cdot\boldsymbol{r} + a^2}$$

$$A_1 = (1+\nu)(\boldsymbol{b}\cdot\boldsymbol{t})(\boldsymbol{b}\cdot\boldsymbol{t}')$$

$$A_2 = (b^2 + (\boldsymbol{b}\cdot\boldsymbol{t})^2)(\boldsymbol{t}\cdot\boldsymbol{t}')$$

$$A_2' = (b^2 + (\boldsymbol{b}\cdot\boldsymbol{t}')^2)(\boldsymbol{t}\cdot\boldsymbol{t}')$$

TABLE II. Values of the Fourier coefficients in Eq. (21) for the EAM and MEAM potentials.

Potential	Function	c_0	c_1	d_1	c_2	d_2	c_3	d_3
EAM	f	1.1017	0.0149	−0.7895	0.0082	−0.0634	−0.0331	−0.0078
	g	0.7067		−0.1141				
MEAM	f	0.8390	0.0092	−0.5730	−0.0191	−0.0325	−0.0118	−0.0122
	g	0.7275		−0.1179				

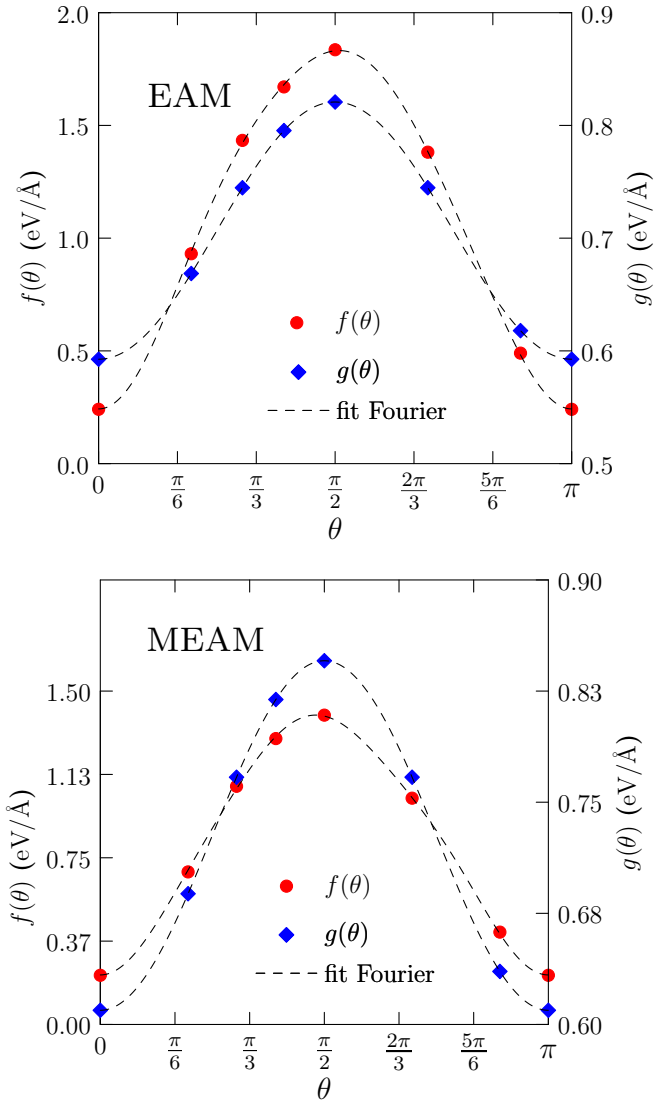

FIG. 16. Dependence of the dislocation core energy terms f and g on dislocation character for (a) EAM and (b) MEAM interatomic potentials.

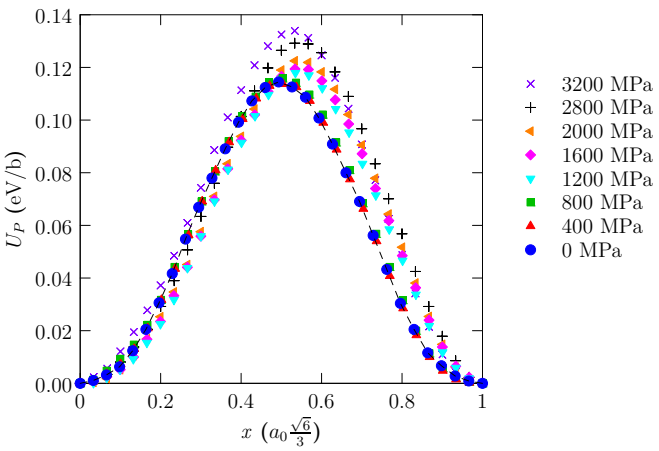

FIG. 17. MEAM potential: Peierls potential variation with stress.

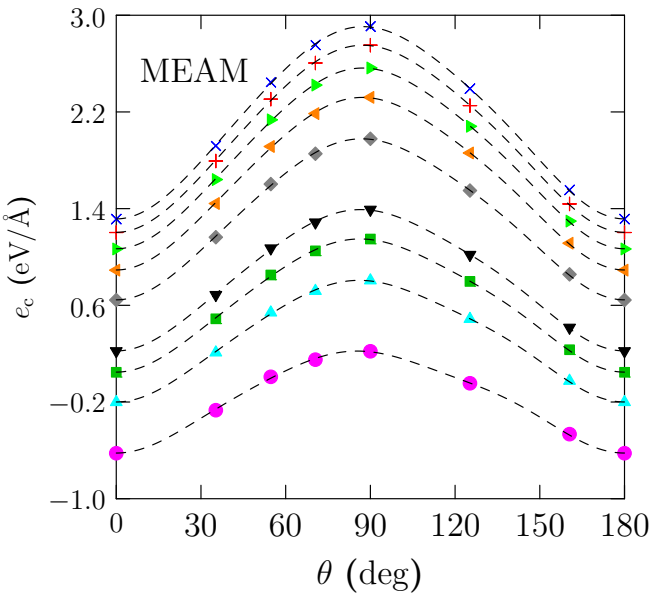

FIG. 18. MEAM potential: Core energy fitting.

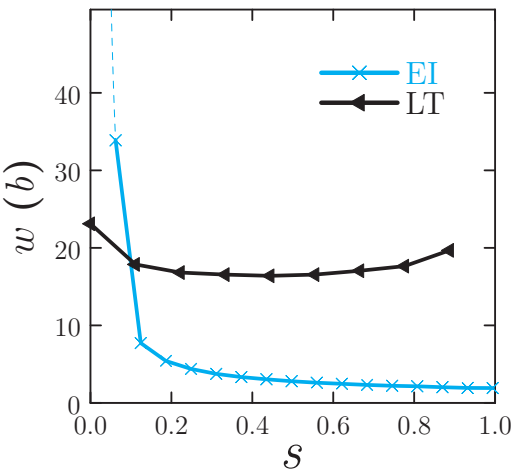

FIG. 19. MEAM potential: Kink separation for EI and LT models.

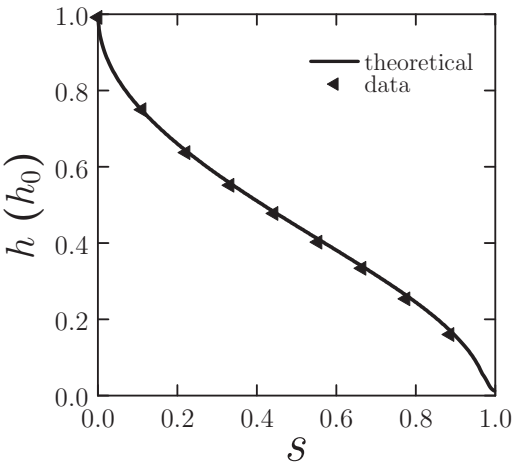

FIG. 20. MEAM potential: Theoretical prediction and simulation results for LT model.

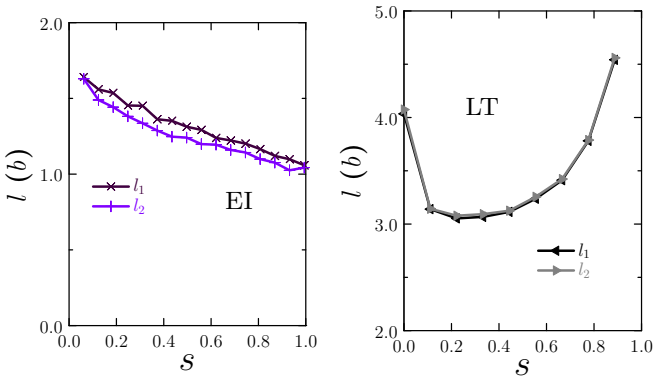

FIG. 21. MEAM potential: Kink widths l_1 and l_2 as a function of stress.

$$A_3 = 2(\boldsymbol{b}\cdot\boldsymbol{u})(\boldsymbol{b}\cdot\boldsymbol{v})\frac{\boldsymbol{t}\cdot\boldsymbol{t}'}{\boldsymbol{u}\cdot\boldsymbol{u}}$$

$$A_3' = 2(\boldsymbol{b}\cdot\boldsymbol{u})(\boldsymbol{b}\cdot\boldsymbol{v}')\frac{\boldsymbol{t}\cdot\boldsymbol{t}'}{\boldsymbol{u}\cdot\boldsymbol{u}}$$

$$A_4 = ((\boldsymbol{b}\cdot\boldsymbol{t})(\boldsymbol{b}\cdot\boldsymbol{v}) + (\boldsymbol{b}\cdot\boldsymbol{t}')(\boldsymbol{b}\cdot\boldsymbol{v}'))(\boldsymbol{t}\cdot\boldsymbol{t}')$$

$$A_5 = 2(\boldsymbol{b}\times\boldsymbol{u})^2\frac{\boldsymbol{t}\cdot\boldsymbol{t}'}{\boldsymbol{u}\cdot\boldsymbol{u}}$$

where $b = \|\boldsymbol{b}\|$. These expressions simplify significantly for perpendicular segments.

2. Interaction energy between two parallel segments

This interaction includes the interaction of segments of pure screw character with one another and the interaction of kink segments of the same kind with one another. As above, the Burgers vector is assumed to be the same for all segments.

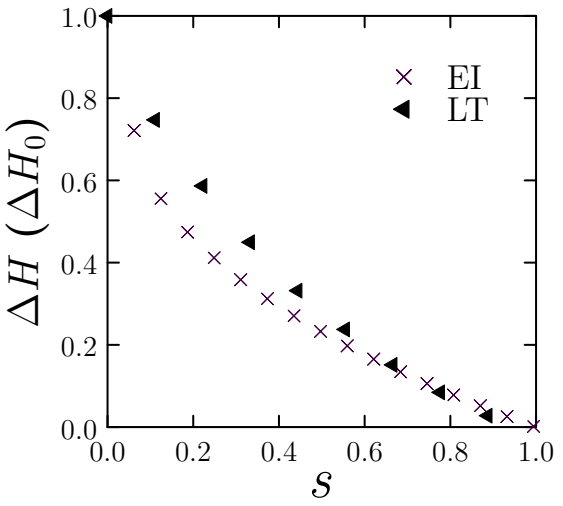

FIG. 22. MEAM potential: Kink-pair activation enthalpy for the EI and LT models.

The interaction energy functional has the form $E^*(\boldsymbol{r}) \equiv E_\parallel(\boldsymbol{r})$:

$$E_\parallel(\boldsymbol{r}) = \frac{\mu}{4\pi(1-\nu)}\Big\{[2b(\boldsymbol{b}\cdot\boldsymbol{r}) - b^2(\boldsymbol{t}\cdot\boldsymbol{r})(3-\nu)] \times \ln\{R_a + \boldsymbol{t}\cdot\boldsymbol{r}\} + R_a b^2(2-\nu) - \frac{R_a}{2}\frac{(\boldsymbol{b}\cdot\boldsymbol{r} - b\boldsymbol{t}\cdot\boldsymbol{r})^2 - a^2b^2(\nu-1)}{R_a^2 - (\boldsymbol{t}\cdot\boldsymbol{r})^2}\Big\}, \tag{C2}$$

where $\boldsymbol{t}$ is the common line tangent to both segments.

APPENDIX D: CALCULATION USING MEAM POTENTIAL

Here we show the series of calculations for the MEAM potential. Except for full atomistic kink-pair enthalpy calculations under stress, the database for the EAM and MEAM potentials is equivalent (cf. Table I). Shown are the variation of Peierls potential with stress (in Fig. 17), Fourier fits of the core energies (Fig. 18), kink separation (in Fig. 19), kink height (Fig. 20), kink widths (in Fig. 21), and activation enthalpy in Fig. 22.

[1] H. Beladi, Q. Chao, and G. S. Rohrer, Acta Mater. **80**, 478 (2014).
[2] C. Marichal, H. Van Swygenhoven, S. Van Petegem, and C. Borca, Sci. Rep. **3**, 2547 (2013).
[3] C. R. Weinberger, B. L. Boyce, and C. C. Battaile, Int. Mater. Rev. **58**, 296 (2013).
[4] J. Bassani, K. Ito, and V. Vitek, Mater. Sci. Eng. A **319–321**, 97 (2001).
[5] D. Kang, D. Baars, T. Bieler, C. Compton, F. Pourboghrat, and A. Mapar, in *Proceedings of the 17th International Conference on RF Superconductivity*, edited by R. E. Laxdal, J. Thomson, and V. RW Schaa (JACoW, Geneva, Switzerland, 2015).
[6] A. Seeger and U. Holzwarth, Philos. Mag. **86**, 3861 (2006).
[7] O. Barrera, D. Bombac, Y. Chen, T. D. Daff, E. Galindo-Nava, P. Gong, D. Haley, R. Horton, I. Katzarov, J. R. Kermode, C. Liverani, M. Stopher, and F. Sweeney, J. Mater. Sci. **53**, 6251 (2018).
[8] D. Rodney and L. Proville, Phys. Rev. B **78**, 104115 (2008).
[9] A. Seeger, J. Phys. IV France **5**, C7-45 (1995).
[10] F. R. Nabarro and M. S. Duesbery, *Dislocations in Solids* (Elsevier, Amsterdam, Netherlands, 2002), Vol. 11.
[11] Y. Zhao and J. Marian, Modell. Simul. Mater. Sci. Eng. **26**, 045002 (2018).
[12] R. Arsenault, Acta Metall. **15**, 501 (1967).
[13] R. Chang, Philos. Mag. **16**, 1021 (1967).
[14] G. Wang, A. Strachan, T. Çağın, and W. A. Goddard III, Phys. Rev. B **68**, 224101 (2003).
[15] L. Dezerald, D. Rodney, E. Clouet, L. Ventelon, and F. Willaime, Nat. Commun. **7**, 11695 (2016).
[16] R. Gröger and V. Vitek, *Materials Science Forum* (Trans Tech Publ, Stafa-Zurich, Switzerland, 2005), Vol. 482, pp. 123–126.
[17] K. Ito and V. Vitek, Philos. Mag. A **81**, 1387 (2001).
[18] M. a.-S. Duesbery and V. Vitek, Acta Mater. **46**, 1481 (1998).

[19] A. Seeger and W. Wasserbäch, Phys. Status Solidi A **189**, 27 (2002).

[20] P. R. Morris and S. Semiatin, Texture, Stress, and Microstruct. **3**, 113 (1979).

[21] C. Marichal, K. Srivastava, D. Weygand, S. V. Petegem, D. Grolimund, P. Gumbsch, and H. V. Swygenhoven, Phys. Rev. Lett. **113**, 025501 (2014).

[22] H. Matsui and H. Kimura, Mater. Sci. Eng. **24**, 247 (1976).

[23] A. Seeger, Mater. Sci. Eng. A **319-321**, 254 (2001).

[24] J. E. Sinclair, J. Appl. Phys. **42**, 5321 (1971).

[25] J. Simmons, S. Rao, and D. Dimiduk, Philos. Mag. A **75**, 1299 (1997).

[26] Y. Tang and M. Ouyang, Nat. Mater. **6**, 754 (2007).

[27] M. R. Gilbert, P. Schuck, B. Sadigh, and J. Marian, Phys. Rev. Lett. **111**, 095502 (2013).

[28] C. R. Weinberger, G. J. Tucker, and S. M. Foiles, Phys. Rev. B **87**, 054114 (2013).

[29] H. Huntington, Proc. Phys. Soc. Sect. B **68**, 1043 (1955).

[30] D. Rodney and L. Proville, Phys. Rev. B **79**, 094108 (2009).

[31] R. Chang and L. Graham, Phys. Status Solidi B **18**, 99 (1966).

[32] V. Celli, M. Kabler, T. Ninomiya, and R. Thomson, Phys. Rev. **131**, 58 (1963).

[33] P. Guyot and J. E. Dorn, Can. J. Phys. **45**, 983 (1967).

[34] K. Edagawa, T. Suzuki, and S. Takeuchi, Phys. Rev. B **55**, 6180 (1997).

[35] J. E. Dorn, J. Mitchell, and F. Hauser, Exp. Mech. **5**, 353 (1965).

[36] J. P. Hirth and J. Lothe, *Theory of Dislocations*, 2nd ed. (Wiley, New York, 1982).

[37] H. Koizumi, H. Kirchner, and T. Suzuki, Acta Metall. Mater. **41**, 3483 (1993).

[38] H. Koizumi, H. O. Kirchner, and T. Suzuki, Philos. Mag. A **69**, 805 (1994).

[39] L. Proville, L. Ventelon, and D. Rodney, Phys. Rev. B **87**, 144106 (2013).

[40] L. Ventelon, F. Willaime, and P. Leyronnas, J. Nucl. Mater. **386**, 26 (2009).

[41] A. Stukowski, D. Cereceda, T. D. Swinburne, and J. Marian, Int. J. Plast. **65**, 108 (2015).

[42] T. D. Swinburne, S. L. Dudarev, S. P. Fitzgerald, M. R. Gilbert, and A. P. Sutton, Phys. Rev. B **87**, 064108 (2013).

[43] D. Cereceda, A. Stukowski, M. Gilbert, S. Queyreau, L. Ventelon, M.-C. Marinica, J. Perlado, and J. Marian, J. Phys.: Condens. Matter **25**, 085702 (2013).

[44] M.-C. Marinica, L. Ventelon, M. Gilbert, L. Proville, S. Dudarev, J. Marian, G. Bencteux, and F. Willaime, J. Phys.: Condens. Matter **25**, 395502 (2013).

[45] H. Park, M. R. Fellinger, T. J. Lenosky, W. W. Tipton, D. R. Trinkle, S. P. Rudin, C. Woodward, J. W. Wilkins, and R. G. Hennig, Phys. Rev. B **85**, 214121 (2012).

[46] G. Henkelman, G. Jóhannesson, and H. Jonsson, *Methods for Finding Saddle Points and Minimum Energy Paths* (Kluwer Academic Publishers, New York, USA, 2000), Chap. 10, pp. 269–300.

[47] S. Plimpton, J. Comput. Phys. **117**, 1 (1995).

[48] T. A. Arias and J. D. Joannopoulos, Phys. Rev. Lett. **73**, 680 (1994).

[49] W. Cai, V. V. Bulatov, J. Chang, J. Li, and S. Yip, Phys. Rev. Lett. **86**, 5727 (2001).

[50] W. Cai, V. V. Bulatov, J. Chang, J. Li, and S. Yip, Philos. Mag. **83**, 539 (2003).

[51] M. Hossain and J. Marian, Acta Mater. **80**, 107 (2014).

[52] K. Kang, V. V. Bulatov, and W. Cai, Proc. Nat. Acad. Sci. USA **109**, 15174 (2012).

[53] W. Cai, A. Arsenlis, C. R. Weinberger, and V. V. Bulatov, J. Mech. Phys. Solids **54**, 561 (2006).

[54] L. Dezerald, L. Ventelon, E. Clouet, C. Denoual, D. Rodney, and F. Willaime, Phys. Rev. B **89**, 024104 (2014).

[55] L. Dezerald, L. Proville, L. Ventelon, F. Willaime, and D. Rodney, Phys. Rev. B **91**, 094105 (2015).

[56] A. Brailsford, Phys. Rev. **139**, A1813 (1965).

[57] D. Caillard and J.-L. Martin, *Thermally Activated Mechanisms in Crystal Plasticity* (Elsevier, Oxford, UK, 2003), Vol. 8.

[58] X. W. Zhou, R. B. Sills, D. K. Ward, and R. A. Karnesky, Phys. Rev. B **95**, 054112 (2017).

[59] W. H. Press, B. P. Flannery, S. A. Teukolsky, and W. T. Vetterling, *Numerical Recipes Book (PASCAL)*, (Cambridge University Press, Cambridge, 1990).

[60] S. Fitzgerald, Sci. Rep. **6**, 39708 (2016).

[61] V. P. Zhdanov, Phys. Lett. A **383**, 744 (2019).

[62] D. Cereceda, M. Diehl, F. Roters, D. Raabe, J. M. Perlado, and J. Marian, Int. J. Plast. **78**, 242 (2016).

[63] U. Kocks, A. Argon, and M. Ashby, Prog. Mater. Sci. **19**, 110 (1975).

[64] C. A. Sawyer, J. W. Morris, Jr., and D. C. Chrzan, Phys. Rev. B **87**, 134106 (2013).

[65] S. Das and V. Gavini, J. Mech. Phys. Solids **104**, 115 (2017).

[66] P.-A. Geslin and D. Rodney, Phys. Rev. B **98**, 174115 (2018).